CHEMISTRY
A European Journal

A Journal of
ChemPubSoc Europe

Accepted Article

Title: Microwave-assisted synthesis of ZnO-rGO core-shell nanorod hybrids with photo- and electro-catalytic activity

Authors: Arpita Jana and Duncan Gregory

To be cited as: *Chem. Eur. J.* 10.1002/chem.202000535

Link to VoR: http://dx.doi.org/10.1002/chem.202000535

Supported by
ACES

WILEY-VCH

10.1002/chem.202000535

WILEY-VCH

Microwave-assisted synthesis of ZnO-rGO core-shell nanorod hybrids with photo- and electro-catalytic activity

Arpita Jana[a] and Duncan H. Gregory *[a]

Abstract: The unique two-dimensional structure and surface chemistry of reduced graphene oxide (rGO) along with its high electrical conductivity can be exploited to modify the electrochemical properties of ZnO nanoparticles (NPs). ZnO-rGO nanohybrids can be engineered in a simple new two-step synthesis, which is both fast and energy-efficient. The resulting hybrid materials show excellent electrocatalytic and photocatalytic activity. The structure and composition of the as-prepared bare ZnO nanorods (NRs) and the ZnO-rGO hybrids have been extensively characterised and the optical properties subsequently studied by UV-Vis spectroscopy and photoluminescence (PL) spectroscopy (including decay life time measurements). The photocatalytic degradation of Rhodamine B (RhB) dye is enhanced using the ZnO-rGO hybrids as compared to bare ZnO NRs. Further, potentiometry comparing ZnO and ZnO-rGO electrodes reveals a featureless capacitive background for an Ar-saturated solution whereas for an O_2-saturated solution a well-defined redox peak was observed using both electrodes. The change in reduction potential and significant increase in current density demonstrates that the hybrid core-shell NRs possess remarkable electrocatalytic activity for the oxygen reduction reaction (ORR) as compared to NRs of ZnO alone.

Introduction

High surface area semiconducting oxide nanoparticles (NPs) have received significant attention in heterogeneous catalysis. Among these, ZnO NPs are particularly interesting because of arelatively large band gap (3.37 eV) and a high exciton binding energy of 60 meV at room temperature.[1] ZnO has a tendency to form several exotic morphologies, and ZnO NRs have exhibited interesting dimension-correlated electronic and optical properties.[2] Meanwhile, graphene and close derivatives have excellent mechanical and electrical properties, high thermal conductivity, superb chemical stability, often a large specific surface area and transparency up to*ca.* 90%.[3] Overall the impressive properties of such 2D carbons can be exploited in applications such as biosensors,[4] supercapacitors[5] and anodes in Lithium Ion batteries (LIBs).[6] Although single layer graphene is extremely difficult to manipulate, few layer graphene materialshave already proved very effective as catalysts.[7]

In this work we consider the synthesis and properties of ZnO NRs coated with reduced graphene oxide (rGO) and the applicability of these materials as catalysts for water splitting and dye degradation. Such a ZnO-rGO hybrid is an interesting prospect in terms of possible synergic properties since the drawbacks commonly associated with ZnO NPs alone, such as low conductivity, could be overcome if combined effectively with a 2D carbon (derivative). Conversely, the layer stacking tendency of rGO sheets could be mitigated by forming an appropriate hybrid such as one with ZnO NPs. We have used solution processing followed-by microwave (MW) heating in the solid state to synthesise ZnO-rGO NR hybrids. Carefully designed MW synthesis can be highly effective since the heating process is fast, volumetric and energy-efficient.[8]

Two very different approaches to the solution synthesis of ZnO-graphene/rGO hybrids have been taken previously; one involves functionalization of ZnO NPs so that they attach to the GO before the latter is reduced.[9] In this first approach, initially the NPs are prepared and then functionalised with positively charged groups (mainly amines) so that they can interact electrostatically with the negatively charged groups in GO.[10] The other synthesis option involves the *in-situ* tethering of a Zn^{2+} precursor to the negative functional groups on the surface of GO (forming Zn-O-C bonds) followed by reduction of both components. In this process, graphene (or rGO) detached from the GO layers through a chemical delamination process, encapsulates the growing ZnO particles, resulting in quasi-core–shell NPs.[11]The reduction of GO is usually performed hydrothermally and/or by using hydrazine as a chemical reductant.[9],[10] However, our objective in this work was to maximise the energy efficiency and simplicity of the reaction process by reducing the GO using microwave irradiation. In this context, it is worth noting that Kumar *et al.* successfully prepared composites of ZnO particles deposited on/in arrays of graphene sheets in a MW-assisted process; Zn^{2+} was attached to exfoliated graphene *via* assumed Zn-O-C interactions and then irradiated in a domestic MW oven.[12]

Oxygen is the one of the most plentiful elements in the Earth's crust and the oxygen reduction reaction (ORR) is considered central to life processes. Technologically it is crucial in energy conversion and storage systems such as alkaline fuel cells and metal-air batteries respectively.[13] NPs of noble metals and alloys with controlled facets are widely used as electrocatalysts for the ORR in fuel cells, but their high cost and scarcity places a restriction on the commercialization of fuel cells for automotive applications. Consequently, given the reduced costs, transition metal oxides and associated hybrids are extremely attractive alternatives in cases where they can demonstrate high catalytic activity. Nanoscale ZnO is an example of a metal oxide that meets the activity and cost criteria and given its low toxicity has minimal environmental impact. Moreover, the rich defect chemistry of ZnO in nanoparticular form leads to emissions beyond the UV and into the visible region. These various vacancies, interstitials and substitutional defects can be controlled via synthesis/processing and the ability to trap charge and extend carrier lifetimes has important implications for photo- and electro-catalysis.[14-16] Hybrids of ZnO NPs and rGO would

[a] Dr. Arpita Jana , Professor Duncan H.Gregory
WestCHEM School of Chemistry,
University of Glasgow, Glasgow G12 8QQ,
United Kingdom
E-mail: Duncan.Gregory@glasgow.ac.uk

Supporting information for this article is given via a link at the end of the document.

be envisaged to have their own advantages and disadvantages in the context of forming electrodes. For example, graphene has a high electrical conductivity but the fabrication of flexible supercapacitor devices from graphene is not easily achievable, for example, since the linking of sheets produces large increases in internal resistance in as-prepared electrodes.[17] Conversely semiconducting metal oxides have relatively low electrical conductivity but their inherent capacitance can yield a high energy density.[18] So it might be expected that hybrids formed from these ZnO and rGO components could combine to produce high capacitance electrode materials. Some previous work has indicated that composites formed from Mn- and Co-containing oxides with rGO have yielded promising results,[19] but there are very few reports that have considered ZnO-rGO nanohybrids for the ORR and such materials systems have also incorporated other transition metal oxides. For example, Sun *et al*. demonstrated that Co-doped ZnO NPs supported on rGO show better catalytic activity than either the NPs or the rGO sheets themselves.[20] There is precedent for other oxide semiconductor-graphene nanohybrid catalysts for the ORR, however and N-doped TiO_2-graphene shows good ORR electrocatalytic activity.[21]

The work described herein demonstrates that ZnO itself (i.e. undoped with other metals) can act as an ORR electro-catalyst when coupled with rGO in core-shell nanostructures. Indeed without the rGO component, the ORR activity of the ZnO NPs is negligible. Our synthesis route leads consistently to uniform ZnO NRs wrapped with rGO layers, which exhibit not only impressive electrocatalytic activity for the ORR, but also offer outstanding photocatalytic performance in dye degradation.

Results and Discussion

Figure 1 schematically represents the reaction mechanism. The rationale behind the synthesis procedure was to coat the ZnO NPs fully with layers of rGO. Zinc acetate provides a source of Zn^{2+} in the ethanolic solution. GO is suspended in the same solution and offers available functionalities such asepoxy, hydroxyl, carboxyl and carbonyl groups (the latter two predominantly at the sheet edges). These groups offer a means to tether Zn^{2+} to the surface, while retaining oxygen and forming Zn-O-C bonds. After heating the reaction for 2 h at 80 °C under reflux, the partially reduced GO would be anticipated to cover the (anisotropic) ZnO NPs. The subsequent MW treatment (which involves the strong coupling of C-C bonds in graphene layers with the incident MW field to generate heat) would further reduce the partially-reduced GO layers (carbothermally). The advantages of using microwave irradiation for the final reduction step is not only that the process is rapid and energy-efficient but that high quality rGO that is almost free of surface functional groups can be obtained without adding a further chemical reductant. Similarly, the carbon coated zinc salts are thermally decomposed to ZnO under the influence of the microwave field.[12] We assessed the two outcomes of the MW heating process by synthesising “bare” ZnO nanomaterials from a solution of Zn^{2+}without added GO and comparing the respective products.

Figure 2 shows the PXD patterns from the ZnO and ZnO-rGO hybrids. All the narrow, crystalline peaks were matched to hexagonal wurtzite ZnO (ICDD PDF code 36-1451) in both samples. The broad peak centred at 24.01° originates from the (002) plane of rGO.

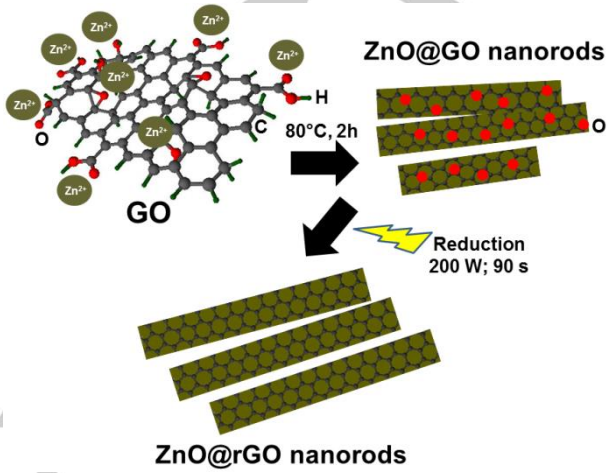

Figure 1. Schematic diagram representing the process for the synthesis of ZnO@rGO NR hybrids.

The intensity of the rGO peak in the PXD pattern is very low compared to the ZnO reflections as would be expected from the lower concentration of more weakly scattering GO used in the synthesis. The position of the broad reflection indicates the successful reduction of GO to rGO[11] and Figure S1(a) and S1(b) show the experimental PXD patterns of GO and rGO respectively for comparison. These patterns highlight the differences between GO and its reduced counterpart. The characteristic (002) peak for GO (Figure S1a) is observed at 11.02 Å which corresponds to an interlayer spacing of 5.21 Å. The wide interplanar distance arises from the introduction of oxygen-containing functional groups on both the faces and edges of the carbon layers. For rGO a very broad peak is observed over a 2θ range of 13.72 - 37.79° (centred at 2θ=25.5°, Figure S1b). A similar broad peak (originating from rGO) is present in the diffractogram from the ZnO-rGO hybrid. The breath of this peak indicates the loss of long range interactions between the stacked carbon layers.[22] No other broad or narrow peaks were present in either of the PXD patterns suggesting the successful formation of phase pure ZnO and the ZnO-rGO hybrid respectively.

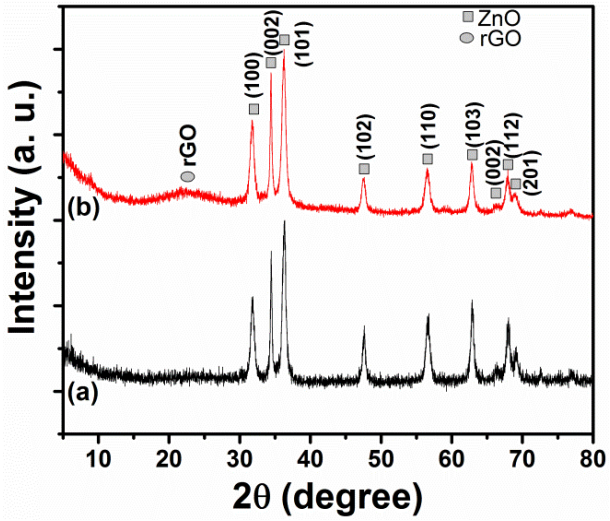

Figure 2. PXD patterns of (a) ZnO and (b) the ZnO-rGO hybrid material prepared by following similar solution/MW synthesis processes.

The transmission electron microscopy (TEM) images show that both the ZnO NPs and the hybrid have rod-like structures (Figure 3a, b). In the ZnO-rGO hybrid, however, the outer surfaces of the nanorods (NRs) are covered with an additional layer up to approximately 1-2 nanometers in thickness (Figure 3c and d). The dimensions of the bare ZnO NRs are typically *ca* 55 nm long and 10 nm wide and both the ZnO and ZnO-rGO rods form with narrow size distributions (Figure 3a and 3c). As might be anticipated from the PXD patterns, TEM confirms that the ZnO NRs are crystalline. The resolution of the fringes shown in the HRTEM images demonstrates that the crystallinity is high within each NR. For example, in the image in Figure 3b, lattice fringes with a spacing of 0.26 nm are clearly visible, which correspond to the (002) lattice planes from Wurtzite-structured ZnO. The dimensions of the coated ZnO NRs are not appreciably different from those of the bare rods and so it can be inferred that the GO does not appear to restrict the growth of the ZnO NRs over the 2 h periods that the solution is heated. In the corresponding selected area electron diffraction (SAED) pattern, the appearance of well-defined spots is further evidence of the crystallinity of the sample. From a comparison of the images in Figure 3(b) and Figure 3(d), it is clear that the outer layers of each of the bare ZnO NRs are also crystalline (given the distinct fringes that can be observed). It is noticeable, however, that the outer layers of the ZnO-rGO NRs do not show the same level of crystallinity, further suggesting that the ZnO NRs are covered by layers of disordered rGO. Closer inspection of the HR-TEM image in Figure 3(d) shows that the rods are coated with thin virtually transparent rGO sheets. SAED patterns were collected for both the ZnO and ZnO-rGO samples in order to make a more complete comparison. The inset SAED patterns in Figure 3(b) and Figure 3(d) indicate that the crystallinity in the samples originates only from the ZnO NRs. In fact, in the rGO coated ZnO NRs the bright spots from the Wurtzite structure are part-obscured by the strong amorphous-type halo from the rGO component of the hybrid material. Additional TEM images of the ZnO-rGO NR hybrid are provided in the supporting information (Figure S2).

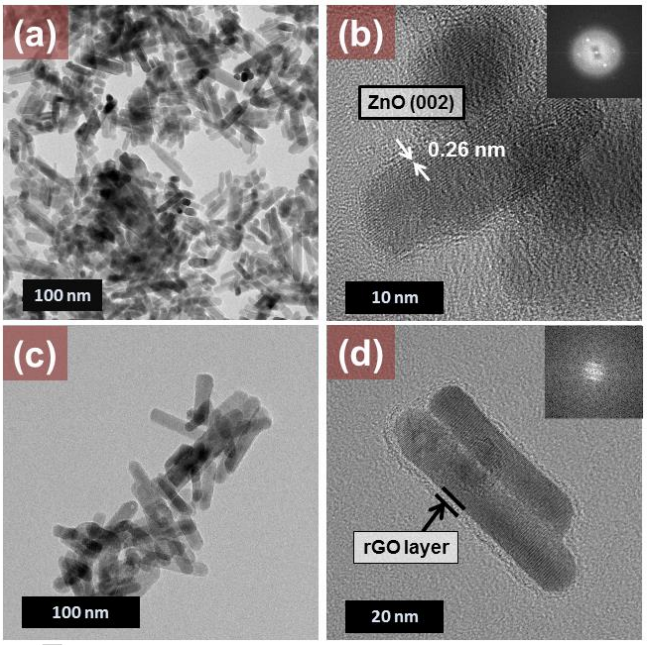

Figure 3. TEM images at lower magnification and high resolution respectively of (a, b) bare ZnO NRs and(c, d) rGO coated ZnO NRs. SAED patterns are shown as insets in (b) and (d).

Figure 4(a) shows typical FTIR spectra of ZnO and ZnO-rGO NRs respectively. The FTIR spectrum of the ZnO-rGO NR hybrids shows only peaks characteristic of C-C bonding without any bands attributable to carboxyl, hydoxyl or other oxygen-containing functional groups, indicating that the GO is converted to rGO in the reduction step of the synthesis. The peak at 1577 cm^{-1} corresponds to the C=C ring stretching vibration.[23] The peak at 1417 cm^{-1} is due to sp^2 hybridized C=C in-plane stretching vibrations. The 877 cm^{-1} peak can be assigned to the A_{1U} out-of-plane stretching mode from the interlayer sp^2bonds of graphene.[24] In addition to the expected rGO peaks, a peak is present at 449 cm^{-1} that likely originates from Zn-O stretching vibrations.[25]

The characteristic FTIR spectrum of GO is depicted in Figure S2. Broad bands are observable at 3400 $cm^{-1}$and can be assigned to the O-H group stretching vibration.[26] Bands at 1411 cm^{-1} and 1384 cm^{-1} are due to the C-O vibration and O-H deformation respectively from a C-OH group, whereas two peaks at 1342 cm^{-1} and 1249 cm^{-1} can be assigned to the COO- symmetric stretch and C-OH stretch respectively.[25] A band at 1107 cm^{-1} can be attributed to an epoxy C-O stretch,[26] whereas bands at 1066 cm^{-1} and 1024 cm^{-1} are due to the carbonyl C-O stretch and the C-O-C stretching vibration respectively. It is these various oxygen-containing groups that are proposed to be the principal contributors to the attachment of Zn^{2+} species to the GO layers in solution.

Figure 4(b) shows the Raman spectra of ZnO and ZnO-rGO NRs excited with a 532.5 nm Ar^+ laser at room temperature. In the ZnO-rGO hybrid, both the Raman active peaks of ZnO and rGO are present, as would be expected. Although many of the peaks that originate from the ZnO NR component are embedded under the higher intensity D and G bands from the rGO shell, the relatively intense ZnO E_2 mode at 440 cm^{-1} is highly visible.

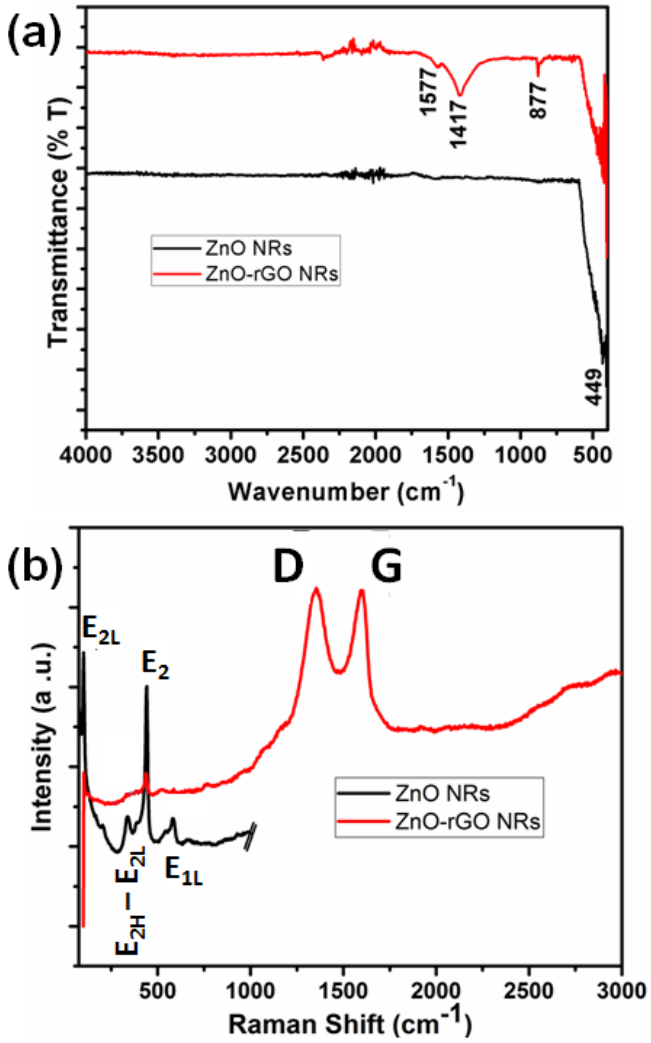

Figure 4. (a) FTIR spectrum (b) Raman spectrum of ZnO and ZnO-rGO NRs.

The carbonaceous D and G bands are present at 1360 cm^{-1} and 1594 cm^{-1} respectively in the hybrid NRs. The G band can be attributed to the first-order scattering from the E_{2g} phonon of sp^2 carbon bonding while the D band is due to the structural defects of disorder-induced modes.[27, 28] There is no 2D band present in the spectrum, which indicates that the surface film is not formed from a single graphene layer – a finding consistent with TEM results. There are some reports of the G band splitting into two sub bands G^+ and G^- due to the strain-induced symmetry breaking that is a consequence of the bending of graphene layers.[11, 29] Although the ZnO-rGO NRs have a core-shell-like structure, we saw no evidence of such splitting (maybe due to the absence of single-layer graphene). Raman spectra are very sensitive to the crystalline nature, structural disorder and defects in crystalline materials and among the bands originating from ZnO, the E_1(LO) mode at 580 cm^{-1}, for example, is likely due to the presence of either oxygen vacancies or oxygen interstitials. The most dominant and sharpest peak observed in the Raman spectrum of ZnO NRs at 440 cm^{-1} is due to the intrinsic Raman-active E_2 mode which is characteristic of the hexagonal wurtzite phase of ZnO.[30] This result is very similar to that noted previously for ZnO-graphene/GO hybrid systems.[9, 11, 31, 32] The defect concentration in rGO can be estimated from the D:G band intensity ratio, I_D/I_G; the higher this ratio is, the higher the resulting defect concentration. In GO itself the I_D/I_G ratio is typically 0.92 whereas in the ZnO-rGO hybrid system the D:G ratio is 1.01, indicating a higher defect concentration in the hybrid.[33] The Raman spectrum of GO is included in the supporting information for comparison (Figure S3).

The E_2 mode consists of two different modes associated with low and high frequencies phonons, E_2 low (E_{2L}) and E_2 high (E_{2H}).[34] The peak at 100 cm^{-1} is due to the E_2 low frequency mode of ZnO, while the 337 cm^{-1} peak can be assigned to the E_2 mode,[30] which consists of two components from low and high-frequency phonons. It was observed that the relative intensity of the ZnO-related peaks in the spectrum of the hybrid is reduced remarkably which reinforces the premise that the ZnO NRs are coated with an rGO layer.

Figure 5(a) shows the nitrogen adsorption/desorption isotherms at 77 K for ZnO and the ZnO-rGO hybrid respectively. The characteristic type IV isotherm, (nonlimiting adsorption at high P/P_0) indicates meso- and macroporous characteristics.[35] The total pore volume of the material was estimated from the level of N_2 adsorption at a relative pressure of approximately 0.909. Native ZnO NRs exhibited a Brunauer-Emmett-Teller (BET) surface area 41±1 $m^2.g^{-1}$ with an average pore volume of 0.17 $cm^3.g^{-1}$ and a mean pore radius of 53.4 Å. The specific surface area increased marginally to 44±1 $m^2.g^{-1}$ in the ZnO-rGO hybrid, which also yielded a pore volume of 0.22 $cm^3.g^{-1}$ and a pore radius of 79.7 Å. Although the surface area is dictated principally by the ZnO NR core, the slight increase in the specific surface area and porosity of the hybrid is perhaps not completely unexpected since the encapsulating shell in the core-shell structure is itself a high surface area material i.e. rGO. Indeed, more generally, increases in surface area are not uncommon after forming rGO hybrids from metal oxides.[36] Figure S4 shows the pore size distribution of ZnO and ZnO-rGO NRs as calculated using the Barrett–Joyner–Halenda (BJH) method from the desorption branch of the isotherm. Both ZnO and ZnO-rGO are mesoporous; the hybrid has a pore size maximum centred at 7.06 nm, whereas the maximum for the ZnO NRs is slightly closer to the mesoporous range (centred at 5.33 nm).

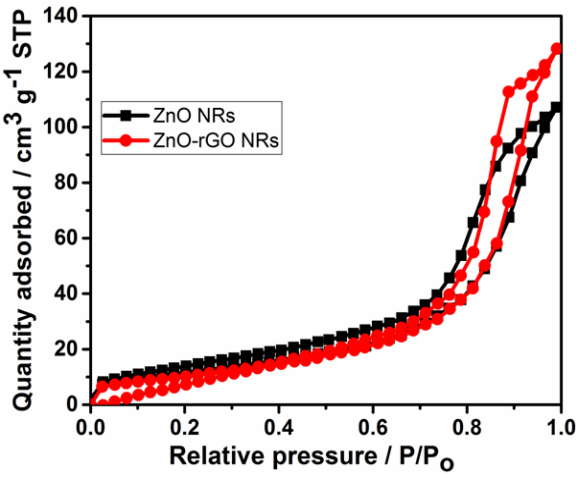

Figure 5.(a) nitrogen adsorption−desorption isotherm curves of ZnO and ZnO-rGO NRs.

The optical properties of the materials were studied by UV-Vis spectroscopy and PL spectroscopy. Figure S6(a) shows the room temperature UV-Vis absorption spectra of the ZnO and ZnO-rGO NRs respectively. The two spectra reveal the characteristic absorption peak of ZnO in both samples at 367 and 364nm for ZnO and ZnO-rGO respectively. This peak can be assigned to the intrinsic band-gap absorption of ZnO due to the electron transitions from the valence band to the conduction band ($O_{2p} \rightarrow Zn_{3d}$). There is no significant shift in this UV-Vis absorption between ZnO and ZnO-rGO samples and the particle sizes are almost identical, as was observed from the TEM images. The DR UV-Vis data were also fitted to the Kubelka-Munk function for a direct band gap semiconductor as a secondary means of confirming the band gaps. The calculated gaps are slightly smaller as obtained from this treatment (the corresponding Tauc plots are shown below in Figure S6(b). From the plots of $(\alpha h\nu)^2$ vs. $h\nu$, the band gap of the ZnO NRs is 3.25 (±0.13) eV while that of the hybrid ZnO-rGO NRs is 3.19 (±0.16) eV.

Figure 6(a) shows the room temperature PL spectra of the ZnO and ZnO-rGO NRs. The PL spectra show two major peaks; one in the UV region and one in the visible region. The peak at *ca.* 390 nm that is present in both samples originates from the excitonic recombination following band edge emission. In the hybrid NRs, it is observed that this band gap emission peak is quenched as compared to the bare ZnO NRs and a broad emission is observed starting at 425 nm and continuing to 630 nm with a maximum centre at 500 nm (2.48 eV). By comparison, the shape of the broad emission peak in the ZnO NR spectrum is quite different and the intensity is much lower. Moreover there is also a small apparently additional peak observed at 441 nm. Both the broad peak (with evidence of fine structure) and the lower intensity peak (at 441 nm) originate from likely oxygen vacancies.[37] Such oxygen deficiency and vacancy formation is known to occur during the formation of ZnO nanostructures and such defects give rise to characteristic emission bands in the PL spectra.[38]

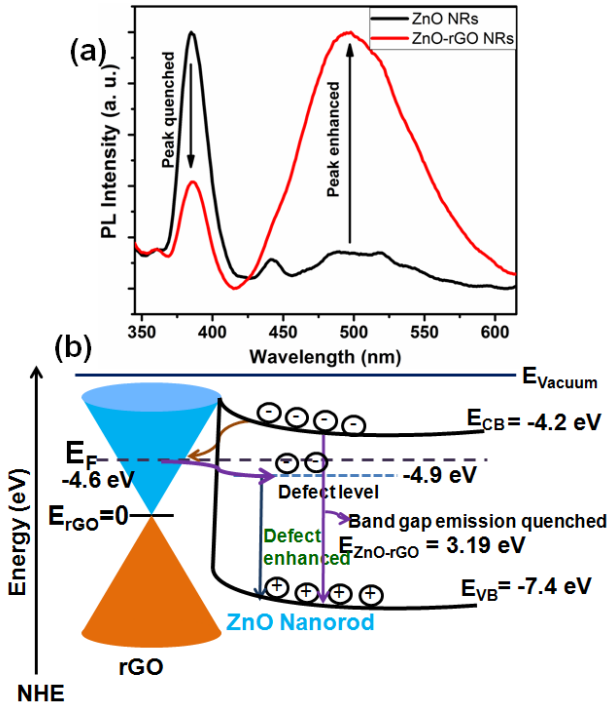

Figure 6. (a) Photoluminescence spectra of ZnO NRs and ZnO-rGO NRs, (b) proposed band diagram of ZnO-rGO hybrid NRs.

The precise nature of the oxygen vacancies in ZnO depends on the fabrication conditions and also on post-fabrication heat treatment regimes.[37] In the hybrid NRs the band gap emission peak of ZnO NRs has been quenched by the presence of rGO, which introduces an additional pathway for the charge carriers. In reality, the vacancy-derived peak located at 441 nm is still present in the ZnO-rGO hybrid PL spectrum (observable by Gaussian peak deconvolution; Figure S7b), obscured by the broader, higher intensity peak that stretches from 425 – 630 nm. Of the five deconvoluted emission peaks, one represents the band gap emission, while the remaining four overlapping peaks emanate from the defect emission. The “bare” ZnO nanorod PL spectrum can be similarly deconvoluted (SI, Figure S7a) and the same pattern of five peaks is observable. Unsurprisingly, the band gap emission peak in the ZnO nanorod spectrum is at virtually the same wavelength as the equivalent emission in the hybrid spectrum (385 nm vs 386 nm). There are slight shifts in the positions of two of the four defect peak maxima to lower wavelengths (at 480 nm and 515 nm respectively), but otherwise the much more significant difference is in the intensity of the defect emission peaks, which are considerably enhanced in the ZnO-rGO hybrid. Previous studies have attributed the blue emissions between 420-480 nm to the presence of oxygen vacancies in nanostructured ZnO.[39, 40] The peaks at 504 nm and 543 nm are due to the $Zn_i \rightarrow V_o$ and CB $\rightarrow V_o$ transitions respectively.[41] We believe that in the hybrid the photo-induced charge carriers from ZnO are trapped by the rGO, quenching the band gap-related emission peak. Relevant to this premise, Kavitha *et al.* observed that two extra emission peaks in the

visible region for a ZnO-rGO system can be attributed to the decay of excitons from the LUMO levels associated with a graphene layer containing epoxy bonds, transferring to the ZnO valence band.[42]Additionally, Pham *et al.* have rationalised near band gap emission quenching in ZnO-decorated thiol functionalised-rGO by an energy level diagram model in which electron transfer takes place from the conduction band of ZnO NPs to graphene.[43] Meanwhile conversely, there is an *increase* in defect emission intensity in the hybrid NRs as compared to the bare ZnO counterparts. This scenario can be explained by the energy-band diagram shown in Figure 6(b).

In the presence of rGO, an electron is transferred from the conduction band of ZnO to the Fermi level (-4.6 eV) of rGO (which has extraordinarily high electron mobility). The highly mobile electron moves from the Fermi level of the rGO to the defect levels (-4.9 eV) of the ZnO; an energetically-favourable process. Thus in the NR hybrids the possibilities for electron-hole recombination decrease and the band gap emission is quenched. By contrast as the density of electrons populating the ZnO defect-related states in the hybrid increases so the intensity from this defect emission also increases.

Son *et al.* also observed comparable PL characteristics in ZnO-graphene systems where when compared to ZnO, the ultraviolet emission peak was quenched and a new defect-related peak appeared in the PL spectrum for the hybrid.[11] In our materials, when the NRs are excited with photon energy higher than the band gap of ZnO, electron-hole pairs are generated. The hole is trapped at the surface of the oxide due to the high surface to volume ratio[44] and the electrons are transferred to the rGO layer. The oxygen vacancies present in ZnO and ZnO-rGO hybrids may be singly ionized or doubly ionized.[45] Magnetic M-H hysteresis measurements were subsequently performed (see below) in order to try and obtain qualitative information regarding the nature of the oxygen vacancies present in the NRs.

Figure 7 shows the fluorescence decay curves at an excitation wavelength of 373 nm. The experimental values for 1 mM solutions of ZnO and ZnO-rGO NRs were fitted to an exponential model, with three decay components, denoted as T_1, T_2 and T_3. The time-dependent PL intensity, $I(t)$is given by the equation 1[46]:

$$I(t) = \sum_{i=1}^{3} A_i e^{-\frac{t}{T_i}} \quad (1)$$

where A_i is the corresponding pre-exponential term for each transition. For the ZnO-rGO NRs, T_1 has the fastest decay (7.1 ns) whereas the slower componentsT_2 and T_3 have identical values (0.63 ns).T_1also has an extremely low probability (5.1×10^{-9} %) which is attributed to the transition from the excited state to the defect state or from the excited state to rGO. This is a non-radiative process.T_2 represents the radiative transition from the excited state to the ground state and is associated with the maximum peak in the PL spectrum.

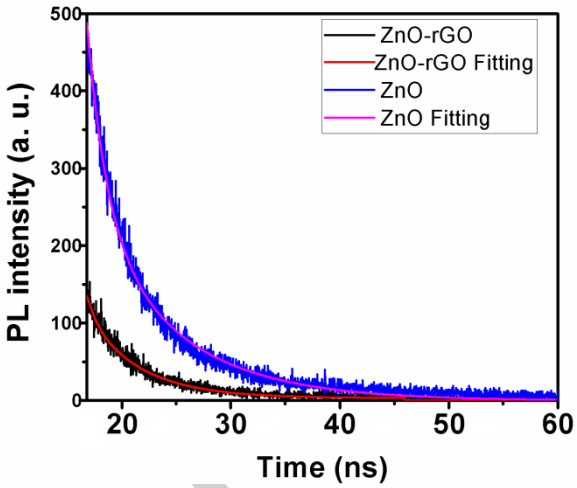

Figure 7: Fluorescence decay of ZnO and ZnO-rGO NRs in ethanol solution.

The final lifetime T_3, represents the defect state to ground state transition in accordance with its minimum PL intensity and this is a radiative process. T_2 and T_3 are has almost equal contributions close to 50%. By comparison, for bare ZnO NRs the three lifetimes are 0.22 ns with a corresponding probability of 1.2×10^{-5}%, (T_1); 4.3 ns with a 0.002% probability (T_2) and 1.04 ns with very close to 100% probability (T_3). The T_1 process in the ZnO NRs is much faster than T_2 and T_3 but has a very low probability and can be attributed to the non-radiative transition from the excited to the defect state. T_2arises from the radiative transition from the ZnO defect state with the minimum PL intensity. T_3 can be attributed to the radiative transition from the excited state to the ground state with the maximum intensity in the PL spectrum. The average lifetime of the ZnO-rGO NR decay is 0.6 ns as opposed to a decay of 1.03 ns for the ZnO NRs. Williams and Kamat observed that the average lifetime of ZnO-GO composite emission decay decreases from 30.2 ± 1.0 ns to 13.7 ± 0.3 ns as the GO concentration is increased.[47] The faster decay in the case of the ZnO-rGO NR hybrid compared to the bare ZnO NRs indicates the introduction of additional charge transfer-induced non-radiative pathways.[48]

Figure 8 shows plot of the magnetization vs. applied field (M vs H) for ZnO and ZnO-rGO NR samples at 300 K. A background correction was performed for both samples. The full hysteresis curve is shown in the supplementary information (Figure S11). Both samples showed well-defined hysteresis loops at 300 K and from the experimental curves it was notable that the ZnO-rGO NRs exhibit an appreciable ferromagnetic response at room temperature. This observation is consistent with the PL curve shows the hybrid has higher defect related emission intensity. Room temperature ferromagnetism can arise in 'pure' ZnO NRs from various kinds of structural defects such as oxygen vacancies, zinc vacancies, zinc interstitials and oxygen interstitials.[45, 49] The peaks observed in the PL spectra of both samples, strongly indicate that oxygen vacancies are present in both cases[45] and that the oxygen vacancy is singly ionized (V^{+}_{O}) given that the materials exhibit ferromagnetic behaviour.[37] Magnetic ordering in ZnO can either be induced by transition

metal doping or can originate from the intrinsic defects present in the wurtzite structure itself; commonly oxygen and/or zinc vacancies (V_O and V_{Zn} respectively). It is often the former that are responsible for low temperature ferromagnetism in ZnO and high temperature annealing typically removes such oxygen vacancies, switching the material into the diamagnetic state.[38]

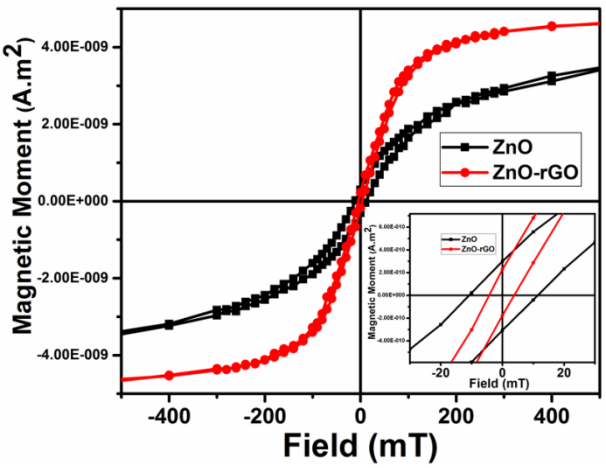

Figure 8. M-H hysteresis curves for ZnO NRs and ZnO-rGO hybrid NRs at 300 K. The bottom left insets shows a magnified section around the origin.

The population of defects is not large and uniform in ZnO NRs, so the magnetization of these materials is much reduced compared to established bulk ferromagnetic oxides, for example.[50] Removal of functional groups from GO causes the formation of defects and distortions in rGO, which has also been reported to lead to ferromagnetic behaviour in rGO itself.[50] Comparing the room temperature M-H response of the two samples, ZnO NRs exhibit a coercive field (H_c) of 10.62mT, a remnant magnetisation of 2.93×10^{-10}A.m^2 and a saturation magnetisation of 4.34×10^{-9} A.m^2 at 300K. By contrast, the ZnO-rGO NRs have a lower coercivity (H_c = 4.34 mT) and remanence (M_r= 2.29×10^{-10} A.m^2), but the saturation magnetisation for the ZnO-rGO hybrid (5.47×10^{-9}A.m^2) is almost twice that of the bare ZnO NRs. In previous work on ZnO NPs enwrapped in graphene, an increase in the value of M_S was observed as the number of defect states in the materials increases.[24] The presence of either oxygen vacancies or zinc vacancies has been documented to be responsible for the ferromagnetism observed in undoped ZnO..[37, 45, 51-53] From the PL spectra it was observed that the defect-related emission intensity increased in the hybrid, which implies a higher defect concentration, likely originating from a V^{+}_O vacancy in ZnO. Consistent with this observation, the hybrid exhibits an increase in the saturation magnetisation. It is not possible from the existing data to evaluate the contribution that the rGO may make to the magnetisation, but one cannot assume that it plays no active role.[50]

In this study we have coated ZnO NRs with rGO layers, where ZnO NRs themselves might be expected to be better catalysts than bulk ZnO due to their higher surface areas. Additionally, then, the rGO layer should improve the electrical conductivity of the materials. Given that a new synthesis approach of chemical/MW reduction was applied to prepare the ZnO-rGO hybrid, it is of interest to contemplate how this methodology might influence the catalytic properties of the materials. The synthetic advantages are that the new process is simple, rapid, cost effective of low environmental impact and can be easily scaled up. The ensuing catalytic performance of the materials is one interesting and important criterion.

Rhodamine B (RhB) is an example of a hazardous industrial organic dye which exists in wastewater and can cause serious environmental problems.[54] We have used this dye as model system to evaluate the photocatalytic activity of bare ZnO NRs as compared to the ZnO-rGO hybrids. From Figure 9(a) it was observed that whereas ZnO NRs required 90 min to achieve 90% decomposition, the ZnO-rGO hybrid dye solutions achieved 100% decomposition in only 45 min. Figure S9(a) shows the UV-Vis absorbance spectra for RhB dye as a function of time under UV light irradiation in the presence of the ZnO-rGOhybrid. The proposed RhB dye degradation process using the ZnO-rGO hybrid is indicated in Figure S9(b). In this process, photocatalytic ZnO NRs generate an electron-hole pair following activation by UV light. The subsequent recombination of this electron-hole pair is the reason behind the lower effectiveness of the ZnO NRs as compared to the ZnO-rGO hybrid. In the latter, rGO inhibits the electron and hole pair recombination, since the electron mobility of rGO assists the selective electron transfer to the rGO layers in preference to electron-hole recombination. This excited electron contributes to the decomposition/reduction of the dissolved O_2 to $\bullet O_2^-$ whereas the hole helps to decompose H_2O to HO^-.[55] The superoxide and HO^- radicals decompose RhB to CO, H_2O and other related products. In addition to limiting the recombination of the electron-hole pair, a large number of charges are available on the hybrid surface which helps to produce huge number of above mentioned radicals. As compared to ZnO NRs themselves, the increases in surface area and porosity of the ZnO-rGO hybrid NRs provide further means to enhance the photocatalytic activity of the catalyst.[56] Figure 9(b) compares the photocatalytic degradation of RhB using the ZnO-rGO NR hybrids to the equivalent process with a commercial Degussa P25, TiO_2-based catalyst, under UV irradiation the hybrid outperforms P25. Given that the ZnO-rGO hybrid has the effect of completely degrading the dye in 40 minutes, it would appear to outperform other similar types of composite and hybrid catalysts. For example, S/N co-doped $CoFe_2O_4$@rGO@TiO_2 nanoparticles were able to photocatalytically degrade RhB dye in 120 min, [57] while zinc oxide crystals combined with few-layered graphene flakes reached 100% RhB degradation in 55 min.[58]

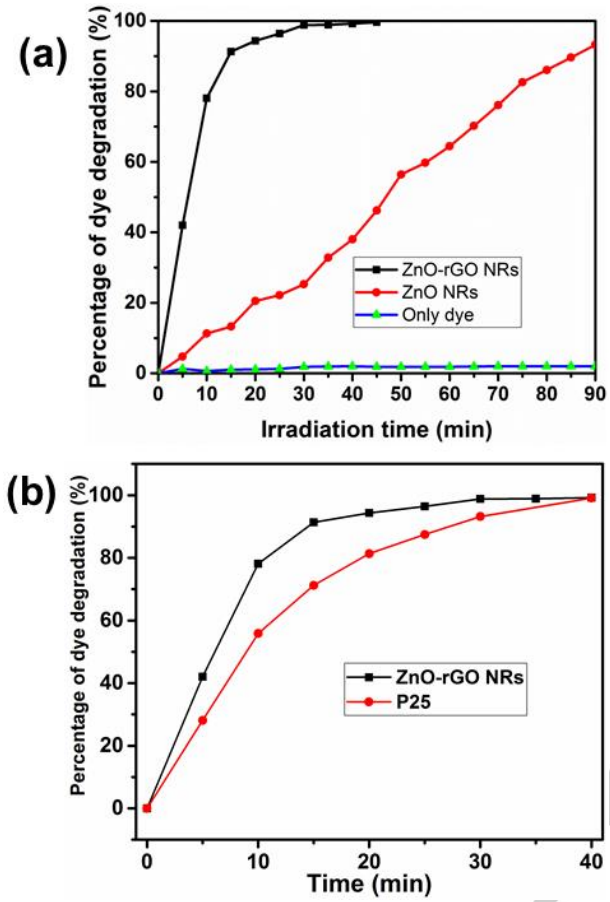

Figure 9. Photodegradation of RhB vs time for:(a) ZnO NRs (red circles), ZnO-rGO NRs (black squares) and RhB dye alone (green triangles); (b) ZnO-rGO NRs (black squares) and commercial Degussa-P25 (red circles).

Figure S8(a,b) depict the cyclic-voltammograms (C-V) curves for ZnO NRs and ZnO-rGO hybrid NRs respectively at scanning rates from 0.05 V s^{-1} to 0.5 V s^{-1} in a potential window of 0.4 – 1.6 V. The basic shape of all these curves is almost the same and there is no obvious distortion in the CV curves as the potential scan rates are increased.

The quasi-rectangular C-V curves, contain no obvious redox peaks and the symmetric shape even at scan rates as high as 0.5 Vs^{-1}, indicate a typical capacitive behaviour with a fast charge-discharge rate and a low contact resistance between electrode and electrolyte.[59]For both samples the obvious increase in current with scan rate suggests that the rate capabilities of the electrodes should be encouraging.[60] For any particular sweep voltage, the hybrid yields a higher current as compared to the ZnO NRs themselves. As an example, Figure S8(c) shows the equivalent voltammograms of ZnO and ZnO-rGO NRs at a sweep voltage of 0.5 V s^{-1}. At every scan rate the hybrid also gives a higher current. Given the higher surface area and porosity of the ZnO-rGO NRs compared to the ZnO NRs, the higher current readings likely result from the higher accessibility of electrolyte ions to the electrode. Improved ion transport and ion storage would lead to higher rate capabilities - as reflected in the high current observed for the hybrid in the voltammograms.[61] Figure S8(d) shows the increase in current response with increasing scan rate, which indicates a surface controlled electrochemical process for the ZnO-rGO hybrid electrode.[62]

For ORR experiments, C-Vs of the ZnO and ZnO-rGO catalyst were performed in Ar- and O_2-saturated aqueous 0.1 M KOH solution at a constant sweep rate of 0.5 Vs^{-1} under ambient conditions. Initially an Ar-saturated solution was prepared that was ensured to be was oxygen free. The resulting profiles observed for both working electrodes within the potential range show no signs of ORR activity (Figure10a, b). When an O_2-saturated solution was adopted, a well-defined cathodic peak corresponding to oxygen reduction was observed at 1.89 V (vs. SCE) for the ZnO-rGO NR electrode. The pure ZnO NR electrode produced a similar reduction peak, but with very low current density (*ca*. an order of magnitude lower) and in this case there was a clear shift of the peak to lower potential (Figure10a). This is due to the high inherent electrical resistance of ZnO NRs, which hinders the electron transfer to oxygen in alkaline solution during the ORR.[20] Thus the ZnO-rGO NR hybrids shows a significant increase in electrocatalytic activity when compared to the ZnO NRs (a positive shift in the ORR potential by 1.81 V and a substantial increase in current density). An enhanced ORR activity for the hybrid materials is expected on grounds of higher surface area, but importantly, the close-contacting outer layer of rGO in the hybrid NRs provides a highly conductive charge transfer pathway.

There are some previous examples of transition metal oxide-rGO hybrids that display ORR activity. In one case, Liu *et al.* showed that the extent of doping in a $NiCo_2S_4$@N/S doped-rGO catalyst was crucial in optimizing the ORR performance,[63] while a hybrid of Mn_3O_4 NPs and nitrogen-doped graphene displayed notable ORR activity at -0.3 V, which was shown to be a four electron process.[64] Similarly, a hybrid formed from $MnCo_2O_4$ and N-doped rGO sheets proved to have better ORR catalytic activity (at 0.91 V) than either of the hybrid's individual components (which demonstrated reduction at reduced positive potentials).[65] It is clear from these and other studies that mixed valent transition metal systems can provide donor-acceptor chemisorption sites for the reversible adsorption of oxygen.

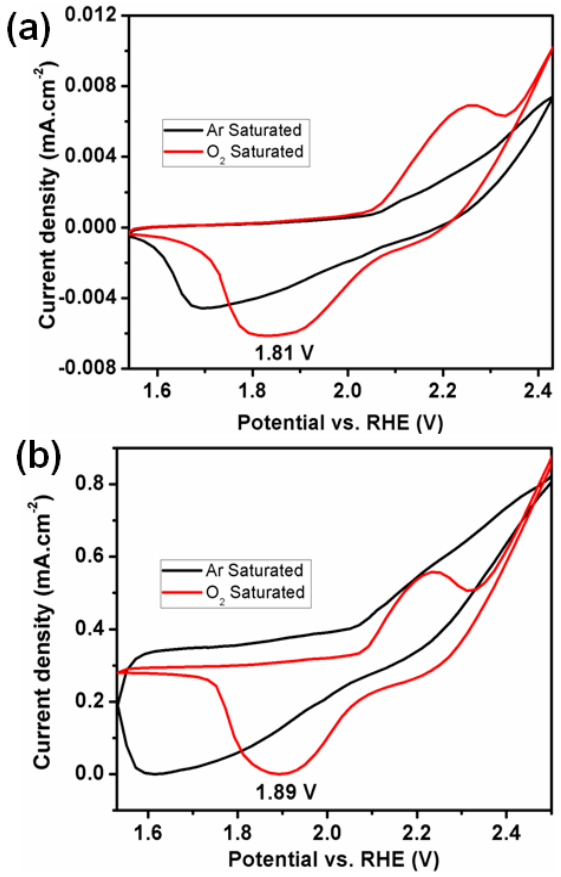

Figure 10. C-V curves of (a)ZnO-rGO and (b) ZnO NRs in Ar-saturated (black) or O_2-saturated (red) 0.1 M KOH solution (sweep rate 0.5 V s^{-1})

The electrical conductivity enabled by facile electron hopping in such mixed-valence systems results in high catalytic activity.[63]In addition, the spinel-carbon hybrids show superior electrical conductivity over the bare metal catalysts themselves arising from synergic effects with the carbon support. These further promote the electrocatalytic activity in such materials. Compared to redox-active, electrically conducting spinel systems, it is not surprising that the catalytic activity of ZnO-rGO is not as high.

Linear sweep voltammetry (LSV) curves were recorded at different rotation speeds, from 200 rpm to 1300 rpm in order to investigate the kinetic characteristics of the ZnO-rGO NR catalyst towards the ORR (Figure11a). As expected, it was observed that the current density increases with increased rotation speed. This is due to the reduced distance, with increasing rotation speed, between the electrolyte and electrode for the gaseous O_2 reactants, shortening the diffusion pathways and accelerating the oxygen diffusion to the electrode.[64] To know more details about the reaction and specifically how many electrons are transferred in the ORR, the electrochemical data were scrutinised by Koutecky-Levich (K-L) analysis and plotted (in SI units; Figure11b) as the reciprocal of the square root of the rotation speeds ($\omega^{-1/2}$) versus the reciprocal of the current density (J^{-1})[65].The number of electrons transferred in oxygen reduction was calculated from the Koutecky−Levich equation (2):

$$\frac{1}{J} = \frac{1}{J_L} + \frac{1}{J_K} = \frac{1}{B\omega^{\frac{1}{2}}} + \frac{1}{J_K} \quad (2)$$

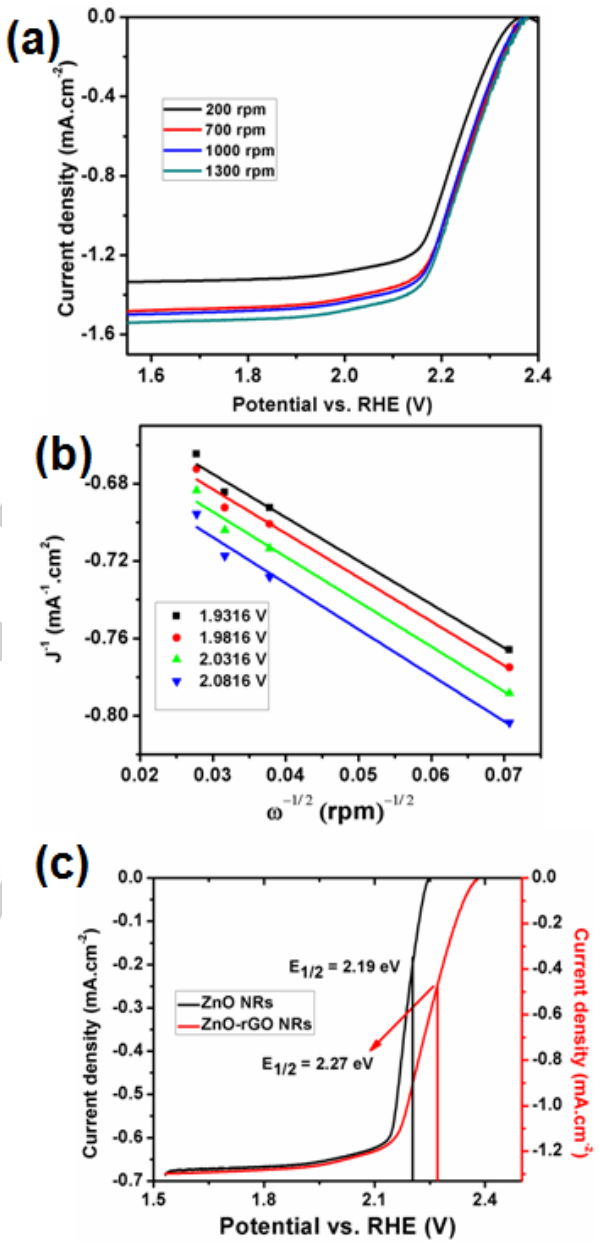

Figure 11.(a) LSV curves of the ZnO-rGO NRs in an O_2-saturated 0.1 M KOH solution at different rotation rates (rpm); (b) Koutecky-Levichplot of J^{-1} vs $\omega^{-1/2}$ for ZnO-rGO NRs at different electrode potentials; (c) Comparison of LSV curves for ZnO and ZnO-rGO NRs in an O_2-saturated 0.1M KOH solution at zero rotation speed.

$$B = 0.62nFC_{O2}D_{O2}{}^{2}/_{3}\ \vartheta(-1)/6 \quad \text{.....(3)}$$

Here, J is the current density, J_L is the diffusion-limiting current density and J_K is the kinetic-limiting current density; ω is the angular velocity; F is the Faraday constant (96485 C mol^{-1}); D_{O2}

is the diffusion coefficient of O_2 in solution (1.9×10^{-5} cm^2s^{-1}); ϑ is the kinetic viscosity (0.01 cm^2s^{-1})[66], C_{O2} is the bulk concentration of oxygen (1.2×10^{-6} mol cm^{-3}) and *n* is number of transferred electrons per O_2 molecule.

The evident linearity of the K-L plots indicates first order reaction kinetics for the ORR. The plots are almost parallel with near-identical gradients, indicating similar electron transfer numbers at all potentials. The calculated values of *n* from the K-L equation were approximately 3.8 - 4.6 in the potential range 1.88 – 2.08 V, suggesting a four electron reduction pathway for the ORR. Figure 11(c) shows that the ZnO-rGO NRs have a higher half-wave potential, $E_{1/2}$ of 2.27 V compared to ZnO NR (2.19 V). These data further substantiate the premise that the ZnO-rGO hybrid is of more promise in terms of ORR activity than ZnO NRs. The more positive potential value at the $E_{1/2}$ for the ZnO-rGO NRs indicates that there are more active sites available at the surface of the ZnO-rGO NRs and fast charge transfer exists between ZnO and rGO. Furthermore the ZnO-rGO NR hybrid electrode has excellent stability, showing no decay in KOH electrolyte by chronoamperometric analysis (SI, Figure S10). Given the electrochemical and PL data, the superior activity of ZnO-rGO NRs towards the ORR is therefore almost certainly due principally to highly efficient interfacial charge transfer and the synergic coupling between the ZnO NR core and the rGO shell, which decreases the activation energy of the dissociative chemisorption of molecular O_2 and facilitates the 4 electron reduction pathways.[67] Incorporation of graphene and derivatives into catalytic composites has a record of improving the electrocatalytic properties of the active materials. Wang *et al*. prepared a PtCu@Graphene Quantum Dot (GQD) composite which has better catalytic activity than commercial Pt black.[68] In the presence of the GQDs, the ORR onset potential for the PtCu catalyst shifted in a positive direction, indicating that the ORR process occurs much more easily when using the hybrid.[69] Similarly, in our system we also observed a positive shift in the half-wave potential of 0.08 V on addition of rGO to ZnO. Alternative approaches to metal-based ORR catalysts include the proposed use of metal-free nitrogen-doped GQDs supported on a graphene sheet substrate (N-GQD/graphene).[70] These catalysts show activity very close to a commercial Pt/C catalyst in alkaline media, while demonstrating excellent durability over 1000 CV cycles in O_2-saturated 0.1 M KOH. Although the ZnO-rGO NR hybrids cannot yet match the level of ORR performance shown by N-GQD/graphene catalysts, our results are comparable to the ORR activity of rGO-supported metal oxides such as the ZnO@rGO materials reported by Sun *et. al.* [71] and Co-doped Ceria/rGO nanocomposites reported by Parwaiz *et al.*[69] Following the lead of the successful catalysts described above, we anticipate that the catalytic activity and durability of the ZnO-rGO nanorod hybrids can be improved by incorporation of hetero atoms (such as nitrogen) into rGO and/or by doping the ZnO nanoparticles with other transition metals. Given that this ZnO-rGO hybrid has a positive onset potential in an alkaline medium and a high electron transfer number (4e from O_2 to H_2O), then it has the potential to act as a non-precious metal alternative to current catalysts at the cathode in alkaline fuel cells. Extended testing would need to be performed to verify this.

The results herein are simply a starting point for further exploration given the limits of the basis ZnO system as a catalyst as described above. The performance of core-shell inorganic-rGO hybrid catalysts can be improved in the first instance by doping the ZnO NR cores with redox-active transition metals to improve transport properties and activity. Moreover ZnO itself is a very flexible choice as the hybrid core. ZnO has a tendency to form a host of different and sometimes exotic morphologies, which are readily tuneable through synthesis and growth parameters. Catalytic activity (and selectivity) will be sensitive to such changes and the ensuing modifications to the surface of the core. Alternatively, in terms of the shell, rGO can be both doped (for example, with nitrogen) and surface-functionalised, which should significantly influence both the electronic structure and topology of the shell surface.

Conclusions

In summary, we have prepared core-shell rGO-coated ZnO nanorods *via* a simple, repeatable two-step process. A mixture of Zn precursor and GO in ethanol is refluxed at 80 °C and the recovered solid irradiated with microwaves at 200 W for 90 s. The rapid, energy-efficient microwave process leads to complete reduction of GO and the formation of uniform, high specific surface area hybrid nanorods. The extensive mesoporosity and superior electrical conductivity engenders a substantial degree of accessibility for sorbed species and facilitates electron transfer. The hybrid core-shell materials demonstrate high photocatalytic activity in the degradation of Rhodamine B and impressive ORR activity. All these performance improvements in the hybridas compared to the equivalent ZnO nanomaterial illustrate the synergic benefits associated with forming rGO core-shell nanostructures and specifically how the approach can considerably improve the stability, durability and catalytic performance of ZnO NPs. Importantly, the morphology of the core material is not altered by the addition of the shell component during the microwave synthesis, yielding predictable hybrid nanoparticles with sizes and shapes dictated by the crystal growth of the inorganic core. The modified synthesis route demonstrated here should be applicable to the preparation of a host of other semiconducting oxide-rGO hybrids and indeed other inorganic core-2D layer shell combinations. The method can pave the way for the design of enhanced photocatalysts, electro-catalysts and functional materials for energy and environmental applications.

Experimental Section

Materials and Methods:

Materials: Zinc Acetate dihydrate (99.99%), sodium hydroxide pellets (98%), H_2SO_4 (>95%), 30% (w/w) solution of H_2O_2, 37% reagent grade HCl and $KMnO_4$ (99%) were used as purchased from Sigma Aldrich.

Sodium nitrate (>99 %) was used as purchased from Alfa Aesar. Graphite powder (99.5%) was purchased from VWR International Ltd. with an indicative particle size less than 50 µm.

Synthesis of Graphene Oxide (GO): GO was synthesized by the Modified Hummers' method.[72]Further details of the procedure are provided in the supplementarty information.

Synthesis of the ZnO-rGO hybrid: Initially, partial reduction was achieved by chemical reduction under alkaline conditions. In brief, 1 g zinc acetate was added to 6 g of NaOH in 150 ml EtOH in a round bottom flux. The solution was stirred for 15 min prior to the addition of 50 ml of a sonicated (10 min) ethanolic solution containing 0.015 g GO. A condenser was fitted to the round bottom flux, and the solution was heated to 80 °C over 15 min and refluxed at 80 °C for 2 h. The resulting suspension was centrifuged and the solid washed with ethanol three times and once with DI water before drying in an oven at 40 °C overnight. The dried powder was placed in a closed glass tube under vacuum and irradiated at 200 W in a modified single mode MW reactor (CEM Discover) under vacuum for 90 sec.

A similar procedure was used for the synthesis of bare ZnO NPs while omitting the addition of GO. Hence, for consistency, the ZnO NPs extracted after reflux were washed, dried and MW heated under identical conditions to the ZnO-rGO material.

Characterization:

Materials Characterizations: Powder X-ray diffraction (PXD) analysis of the products was performed using a Bruker D8Advance diffractometer in Debye-Scherer transmission geometry using Cu Kα radiation (λ = 1.54 Å). The morphology and crystallinity of the product was studied by transmission electron microscopy (TEM; JEOL JEM-2200FS) at an accelerating voltage of 200 kV. The samples were dissolved in ethanol solution and sonicated for 10 min. The resulting suspension was drop cast on a carbon-coated Cu grid (200 mess) and dried overnight at room temperature. Raman data were collected using a Horiba-Jobin Yvon LabRAM HR confocal microscope system (Horiba, Japan) using a 600 mm^{-1} grating and equipped with a Synapse CCD detector. The excitation source (predominantly at 532 nm) was a Nd:YAG second harmonic laser (Ventus 532, Laser Quantum, output power 50 mW - 1.5W). Raman spectra were collected over an effective shift range of 10 – 3000 cm^{-1}. Infra-Red spectra were collected at room temperature (50 scans/sample, 8 cm^{-1} resolution) using a Shimadzu FTIR 8400S with a Pike MIRacle Attenuated total reflectance (ATR) sampling accessory.

Optical properties: The optical properties were studied by UV-Vis spectroscopy and photoluminescence (PL) spectroscopy. The UV-Vis data were measured using an ethanolic suspension of the ZnO NPs and ZnO-rGO NPs respectively with a Shimazdu, UV 2600 spectrometer over a wavelength range of 400-700 nm at room temperature. The photocatalytic study described in the section below was performed with the same UV-Vis instrument. PL studies were performed using a FluroTime300 instrument exciting at 325 nm and measuring over a range of 345 nm - 630 nm. Lifetime fluorescence decays were collected on a Horiba Ultima Extreme instrument with an excitation wavelength of 373 nm.

Magnetic properties: The magnetic properties of the samples were measured in a superconducting quantum interference device (SQUID: Quantum Design, MPMS XL) at 300 K. To probe the external field dependence of the magnetization, the z-direction hysteresis loop was measured at 300K in a range of -3.5 to 3.5 T.

Dye Degradation: The degradation of a 1.5 X 10^{-5} $molL^{-1}$ Rhodamine B (RhB) dye (≥95%, Sigma Aldrich) was monitored by tracing the intensity of its main peak at 544 nm in the UV-Vis spectrum. A small sample of the degrading liquid was withdrawn before and after the irradiation of UV light while under continuous stirring. Each sample taken from the degradation solution was centrifuged immediately and the supernatant was evaluated in terms of the residual dye concentration. The absorption maxima for each sample were measured by UV-Vis spectroscopy. The percentage of dye degradation was calculated according to: $(C_o\text{-}C)/C_o$ X 100, where C_o is the initial concentration and C is the concentration of the RhB dye at a given time point.

Electrocatalytic Properties: Electrochemical measurements were performed using a Uniscan 3100 potentiostat galvanostat and a 3102 power booster running UiEChem software, over multiple cycles. Electrochemical testing for samples of ZnO NRs or ZnO-rGO NRs (as the working electrode) were performed with three electrode cell systems with Pt wire as the auxiliary electrode and Ag/AgCl as the reference electrode. Cyclic voltammetry (C-V) and galvanometric charge and discharge experiments were conducted with 0.1 M Na_2SO_4(≥99%, Sigma Aldrich) solution as the electrolyte. The working electrodes were prepared by pressing the respective samples into Ni foam without the use of a binder. The electrocatalytic ORR activity of the ZnO NRs and ZnO-rGO NRs was evaluated from (C-V) scans in O_2- and Ar-saturated 0.1 M KOH (≥84%, Merck) solutions within a potential window of 1.73 – 2.43 V at a fixed scan rate of 0.5 Vs^{-1}. For multiple cycles, each measurement curve was recorded once the system was stable and the previous cycle had been completed. O_2- and Ar-saturated solutions were made by passing O_2 and Ar respectively into the alkaline solution for 10 min. Chronoamperometrywas conducted with the ZnO-rGO hybrid in a 0.1 M KOH solution with a current of 0.001 A for 2000 s at ambient temperature. All potentials vs. Ag/AgCl were converted to the RHE value using the Nernst equation (ERHE = $E^{\theta}_{Ag/AgCl}$+ 0.059 pH + $E_{Ag/AgCl}$). For CV experiments we used 2 mg catalyst samples without binder or active carbon.

Acknowledgements

AJ gratefully acknowledges the financial support provided by the award of Commonwealth Rutherford Fellowships, (CSC ID: INRF-2017-144). The authors thank Professor David Birch, University of Strathclyde, Scotland, UK for performing the time-resolved Fluorescence decay experiment. We thank Dr. Mark Symes, University of Glasgow, Scotland, UK for the use of the potentiostat/galvanostat. We are grateful to Prof. Dave Adams, University of Glasgow, Scotland, UK for the use of photoluminescence spectroscopy. We acknowledge Dr. T. S. Basu and S. Andreev, University of Konstanz, Germany for performing TEM and SQUID experiments respectively and for useful scientific discussions.

Keywords:reduced graphene oxide (rGO)•Solution synthesis•Microwave irradiation•Photo-catalyst•Oxygen Reduction Reaction

References

[1] C. Klingshirn, *phys. stat. sol.* **2007**, *244*, 3027–3073.

[2] M. Ding, Z. Guo, L. Zhou, X. Fang, L. Zhang, L. Zeng, L. Xie, H. Zhao, *Crystals* **2018**, *8*, 223.
[3] C. Soldano, A. Mahmood, E. Dujardin *Carbon* **2010**, *48*, 2127 – 2150.
[4] Y. Shao, J. Wang, H. Wu, J. Liu, I. A. Aksay, Y. Lin, *Electroanalysis* **2010**, *22*, 1027 – 1036
[5] M. Wang, L. D. Duong, N. T. Mai, S. Kim, Y. Kim, H. Seo, Y. C. Kim, W. Jang, Y. Lee, J. Suhr, J. Nam, *ACS Appl. Mater. Interfaces* **2015**, *7*, 1348−1354.
[6] P. Guo, H. Song, X. Chen, *Electrochem. Commun.* **2009**, *11*, 1320–1324.
[7] D. Haag, H. H. Kung, *Topics in Catalysis* **2014**, *57*, 762–773.
[8] R. Hoogenboon, T. F. A. Wilms, T. Erdmenger, U. S. Schubert, *Aust. J Chem.* **2009**, *62,* 236-243.
[9] D. Shao, M. Yu, H. Sun, T. Hu, J. lian, S. Sawyer, *Nanoscale* **2013**, *5*, 3664-3667.
[10] W. Zhou, J. Zhu, C. Cheng, J. Liu, H. Yang, C. Cong, C. Guan, X. Jia, H. J. Fan, Q. Yan, C. M. Li, T. Yu, *Energy Environ. Sci.* **2011**, *4*, 4954-4961.
[11] D. I. Son, B. W. Kwon, D. H. Park, W.-S. Seo, Y. Yi, B. Angadi, C.-L. Lee, W. K. Choi, *Nat. Nanotechnol.* **2012**, *7*, 465.
[12] R. Kumar, R. K. Singh, A. R. Vaz, S. A. Moshkalev, *RSC Adv.***2015**, *5*, 67988-67995.
[13] C. Song, J. Zhang, in *PEM Fuel Cell Electrocatalysts and Catalyst Layers: Fundamentals and Applications* (Ed.: J. Zhang), Springer London, London, **2008**, pp. 89-134.
[14] S. Kasap, I. I. Kaya, S. Repp, E. Erdem, Nanoscale Adv., 2019, 1, 2586-2597.
[15] E. Erdem, *J. Alloys Compd.*, **2014**, *605*, 34–44.
[16] J. Peter, E. Erdem, *Phys. Status Solidi (RRL)*, **2011**, *5*, 56–58
[17] Y. Shao, M. F. El-Kady, L. J. Wang, Q. Zhang, Y. Li, H. Wang, M. F. Mousavi, R. B. Kaner, *Chem. Soc. Rev.* **2015**, *44*, 3639-3665.
[18] A. A. Ensafi, E. Heydari-Soureshjani, B. Rezaei, *Chem. Eng. J* **2017**, *330*, 1109-1118.
[19] S. Choi, C. Kim, J. M. Suh, H. W. Jang, *Carbon Energy* **2019**, *1*, 85-108.
[20] Y. Sun, Z. Shen, S. Xin, L. Ma, C. Xiao, S. Ding, F. Li, G. Gao, *Electrochim. Acta* **2017**, *224*, 561-570.
[21] W. Yuan, J. Li, L. Wang, P. Chen, A. Xie, Y. Shen, *ACS Appl. Mater. Interfaces* **2014**, *6*, 21978-21985.
[22] L. Zhang, L. Du, X. Cai, X. Yu, D. Zhang, L. Liang, P. Yang, X. Xing, W. Mai, S. Tan, Y. Gu, J. Song, *Physica E: Low-dimensional Systems and Nanostructures* **2013**, *47*, 279-284.
[23] B. D. Ossonon, D. Bélanger, *RSC Adv.* **2017**, *7*, 27224-27234.
[24] A. Jana, E. Scheer, *Langmuir* **2018**, *34*, 1497–1505.
[25] M. Ahmad, E. Ahmed, Z. L. Hong, J. F. Xu, N. R. Khalid, A. Elhissi, W. Ahmed, *Appl. Surf. Sci.* **2013**, *274*, 273-281.
[26] Y. Feng, Y. Zhang, X. Song, Y. Wei, V. S. Battaglia, *Sustain. Energy & Fuels* **2017**, *1*, 767-779.
[27] A. C. Ferrari, D. M. Basko, *Nat. Nanotechnol.***2013**, *8*, 235-246.
[28] J. Wu, M. Lin, X. Cong, H. Liu, P. Tan, *Chem. Soc. Rev.*, **2018**, *47*, 1822-1873.
[29] M. M. Tavakoli, H. Aashuri, A. Simchi, Z. Fan, *Phys. Chem. Chem. Phys.* **2015**, *17*, 24412-24419.
[30] R. Cuscó, E. Alarcon-Llado, J. Ibáñez, L. Artús, J. Jiménez, B. Wang, M. J. Callahan, *Phys. Rev. B* **2007**, *75*, 165202.
[31] C. Yang, L. Hu, H. Zhu, Y. Ling, J. Tao, C. Xu, *J. Mater. Chem. B*, **2015**, *3*, 2651–2659.
[32] R. Paul, R. N. Gayen, S. Biswas, S. Venkataprasad Bhat, R. Bhunia, *RSC Adv.*, **2016**, *6,* 61661–61672.
[33] B. Seger, P. V. Kamat, *J. Phys. Chem. C* **2009**, *113*, 7990-7995.
[34] F. J. Manjóna, B. Marí, *J Appl. Phys.* 2005, **97**, 053516.
[35] X. Bai, C. Sun, D. Liu, X. Luo, D. Li, J. Wang, N. Wang, X. Chang, R. Zong, Y. Zhu, *Appl. Catal. B: Environmental* **2017**, *204*, 11-20.
[36] K. B. Babitha, J. Jani Matilda, A. Peer Mohamed, S. Ananthakumar, *RSC Adv.* **2015**, *5*, 50223-50233.
[37] A. Jana, P. Sujatha Devi, A. Mitra, N. R. Bandyopadhyay, *Mater. Chem. Phys.* **2013**, *139*, 431-436.
[38] A. Jana, N. R. Bandyopadhyay, P. Sujatha Devi, *Solid State Sci.* **2011**, *13*, 1633-1637.
[39] W. Cheng, P. Wu, X. Zuo, T. Xiao, *J. Appl. Phys.* 2006, **100**, 054311.
[40] L. Zhao, S. Sun, *CrystEngComm.* **2011**, ***13,*** 1864.
[41] S. Vempati, J. Mitra, P. Dawson, *Nanoscale Res. Lett.* **2012**, *7*, 470.
[42] M. K. Kavitha, H. John, P. Gopinath, R. Philip, *J. Mater. Chem. C* **2013**, *1*, 3669-3676.
[43] C. V. Pham, S. Repp, R. Thomann, M. Krueger, S. Weber, E. Erdem, *Nanoscale* **2016**, *8*, 9682-9687.
[44] W. Guo, S. Xu, Z. Wu, P. N. Wang, P. M. M. T. Loy, P. S. Du, *Small* **2013**, *9*, 3914-3914.
[45] B. Panigrahy, M. Aslam, D. S. Misra, M. Ghosh, D. Bahadur, *Adv. Funct. Mater.* **2010**, *20*, 1161-1165.
[46] J. R. Lakowicz, *Principles of Fluorescence Spectroscopy*, Springer, Boston, MA, **2006**.
[47] G. Williams, P. V. Kamat, *Langmuir* **2009**, *25*, 13869-13873.
[48] M. K. Kavitha, P. Gopinath, H. John, *Phys. Chem. Chem. Phys.* **2015**, *17*, 14647-14655.
[49] W. Liu, W. Li, Z. Hu, Z. Tang, X. Tang, *J. Appl. Phys.* **2011**, *110*, 013901.
[50] K. Thiyagarajan, M. Muralidharan, K. Sivakumar, *Journal of Materials Science: Materials in Electronics* **2018**, *29*, 7442-7452.
[51] Z. Chen, X.X. Li, G. Du, N. Chen, A.Y.M. Suen, *J. Lumin.* **2011**, *131*, 2072.
[52] X. Zuo, S. Yoon, A. Yang, W. Duan, C. Vittoria, V. Harris, *J. Appl. Phys.* **2009**, *105*, 07C508.
[53] D. Gao, Z. Zhang, J. Fu, Y. Xu, J. Qi, D. Xue, *J. Appl. Phys*., **2009**, *105*, 113928.
[54] J. Rochat, P. Demenge, J. C. Rerat, *Toxicological European research. Recherche europeenne en toxicologie* **1978**, *1*, 23-26.
[55] G. Rajender, J. Kumar, P. K. Giri, *Appl. Catal.s B: Environmental* **2018**, *224*, 960-972.
[56] S. K. Mandal, K. Dutta, S. Pal, S. Mandal, A. Naskar, P. K. Pal, T. S. Bhattacharya, A. Singha, R. Saikh, S. De, D. Jana, *Mater. Chem. Phys.* **2019**, *223*, 456-465.
[57] F. Wei, H. Wang, W. Ran, T. Liu, X. Liu, *RSC Adv.*, **2019**, *9*, 6152-6162.
[58] W. Tie, S. S. Bhattacharyya, Y. Wang, W. He, S. H. Lee, *J. Photochem. Photobio. A: Chem*. **2017**, *348*, 89–95.
[59] A. Bhirud, S. Sathaye, R. Waichal, C.-J. Park, B. Kale, *J. Mater. Chem. A* **2015**, *3*, 17050-17063.
[60] J. Wang, Z. Gao, Z. Li, B. Wang, Y. Yan, Q. Liu, T. Mann, M. Zhang, Z. Jiang, *J. Solid State Chem.* **2011**, *184*, 1421-1427.
[61] Z. Li, P. Liu, G. Yun, K. Shi, X. Lv, K. Li, J. Xing, B. Yang, *Energy* **2014**, *69*, 266-271.
[62] R. Ahmad, N. Tripathy, M.-S. Ahn, K. S. Bhat, T. Mahmoudi, Y. Wang, J.-Y. Yoo, D.-W. Kwon, H.-Y. Yang, Y.-B. Hahn, *Sci. Rep.* **2017**, *7*, 5715.
[63] Q. Liu, J. Jin, J. Zhang, *ACS Appl. Mater. Interfaces* **2013**, *5*, 5002-5008..
[64] K. Maiti, J. Balamurugan, S. G. Peera, N. H. Kim, J. H. Lee, *ACS Appl. Mater. Interfaces* **2018**, *10*, 18734-18745.
[65] R. Liu, D. Wu, X. Feng, K. Müllen, *Angew. Chem. Int. Ed.* **2010**, *49*, 2565-2569.
[66] S. Wang, D. Yu, L. Dai, D. W. Chang, J.-B. Baek, *ACS Nano* **2011**, *5*, 6202-6209.
[67] H. Yin, H. Tang, D. Wang, Y. Gao, Z. Tang, *ACS Nano* **2012**, *6*, 8288-8297.
[68] L. Wang, C. Hu, Y. Zhao, Y. Hu, F. Zhao, N. Chen, L. Qu, *Carbon* **2014**, *74*, 170 –179.
[69] S. Parwaiz, K. Bhunia, A. K. Das, M. M. Khan, D. Pradhan, *J. Phys. Chem. C* **2017**, *121*, 20165−20176.
[70] Y. Liu, P. Wu, *ACS Appl. Mater. Interfaces* **2013**, *5*, 3362−3369.
[71] L. Zhao, S. Sun, *CrystEngComm.* **2011**, *13***,** 1864.
[72] W. S. Hummers, R. E. Offeman, *J. Am. Chem. Soc.* **1958**, *80*, 1339-1339.

10.1002/chem.202000535

WILEY-VCH

Entry for the Table of Contents (Please choose one layout)

Layout 1:

FULL PAPER

Text for Table of Contents

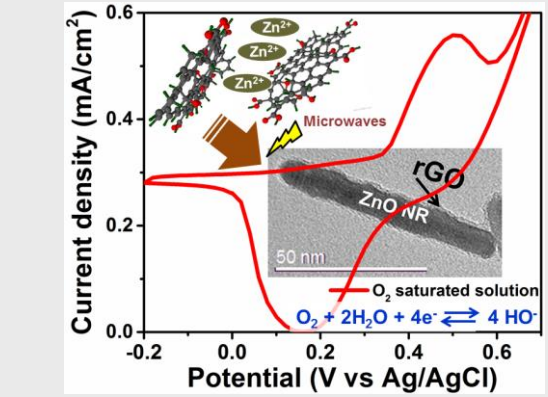

Arpita Jana and Duncan H. Gregory

Page No. – Page No.

Title:Microwave-assisted synthesis of ZnO-rGO core-shell nanorod hybrids with photo- and electro-catalytic activity

Text for Table of Contents:

ZnO-rGO core-shell nanorods have been prepared by a new two-step approach involving solution heating and rapid microwave irradiation. The hybrid possesses extraordinary electrocatalytic and photocatalytic activity to the oxygen reduction reaction and RhB dye degradation respectively.